Microstructural design of ceramics for bone regeneration

Adrián del Valle García, Dominique Hautcoeur, Anne Leriche, Francis Cambier, Carmen Baudin

Microstructural design of ceramics for bone regeneration

Adrián del Valle García[a], Dominique Hautcoeur[b], Anne Leriche[c], Francis Cambier[b], Carmen Baudín[a,*]

[a] Instituto de Cerámica y Vidrio, CSIC, Kelsen 5, 28049, Madrid, Spain
[b] Belgian Ceramic Research Centre, Avenue Gouverneur Cornez 4, B-7000, Mons, Belgium
[c] Univ.Polytechnique Hauts-de-France, EA 2443 - LMCPA - Laboratoire des Matériaux Céramiques et Procédés Associés, F-59313, Valenciennes, France

A B S T R A C T

Dense tricalcium phosphate, $Ca_3(PO_4)_2$ (TCP) – diopside, $CaMg(SiO_3)_2$, composites present better mechanical properties than single phase TCP. In this work, it is investigated whether the mechanical behaviour improvement by diopside is maintained in porous scaffolds.

The processing parameters to obtain cylinders with ≈ 50% of aligned pores of elliptical cross sections with major axis up to 100 μm by freeze casting and sintering were established. Pore channels were introduced in the green specimens by laser ablation. After sintering, the diameter of the cross sections of the channels was ≈ 700 μm. The ceramic composite microstructure was constituted by a substructure of small diopside particles (27 μm) and dense β-TCP zones of larger dimensions (up to 40 μm). Strength values, determined by diametral compression (DCDT) (≈ 2.5–4 MPa) are in the range of strength of cancellous bone. Diopside presents trans-granular fracture, hindering crack propagation from the β-TCP areas and the pores, as occurred in the dense materials.

Keywords:
Tricalcium phosphate
Diopside
Scaffolds
Mechanical properties
Freeze casting

1. Introduction

Currently, bone-associated diseases due to aging or traumas are one of the main problems of public health. As a result, bone is the second most commonly transplanted tissue worldwide, with at least four million operations making use of bone grafts and bone substitute materials annually [1]. Frequently, treatments involve implantation of a temporary or a permanent prosthesis, which is challenging, especially when dealing with large defects.

In principle, xenografts, human allografts and, above all, autografts seem to be suitable solutions. However, all biological-type transplants have drawbacks due to limited amount of donor tissues, donor site morbidity, and/or potential risks of immunological incompatibility and disease transfer.

Therefore, one of the main subjects of materials science is the research on artificial materials for bone tissue substitution and repair.

Calcium orthophosphates $CaPO_4$ (CP) and, in particular tricalcium phosphate $Ca_3(PO_4)_2$, (TCP), have been studied as bone repair materials for about 90 years. They were first considered for clinical application as filler for bone defects in the 1920s [2] and incorporated in dentistry and orthopaedics in the 1980s. Updated reviews on calcium orthophosphates can be found in references [3–5].

The use of granules for bone repair is limited when dealing with load bearing applications. In such cases, it has been proposed the use of engineered structures combining resorbable scaffolds, cells and/or reactive agents as growth factors or antibiotics: tissue engineering constructs (TEC). In the ideal case, these structures would facilitate host cells to deposit extracellular matrix (ECM) and replace the scaffold structure over time. Updated reviews on scaffolds for bone tissue engineering can be found in references [1,5–7].

As highlighted by Hutmacher et al. [7], it is “by no means clear what defines an ideal scaffold”. Since bones of human skeleton have very different dimensions, shapes and structures depending on their functions and locations, synthetic bone grafts of various sizes, shapes, porosity, mechanical strength, composition and resorbability would be necessary [5]. Moreover, it is needed to reach a compromise between incompatible required properties such as mechanical strength and high levels of interconnected porosity to allow colonization by cells, as described below.

It is generally accepted that scaffolds should provide sufficient initial mechanical strength and stiffness to substitute for the mechanical function of the damaged bone until it is regenerated and/or permit cell seeding of the scaffold in vitro without compromising scaffold architecture. However, there is no agreement in the literature about the

target mechanical properties for bone scaffolds [4].

It has been proposed that the ideal scaffold would have a compressive strength comparable to cortical bone, which along the long axis is approximately 100–230 MPa, with a Young's modulus close to 7–30 GPa and a tensile strength of 50–150 MPa. Ideally these mechanical properties have to be complemented by porosity between 60% and 90% and an average pore size larger than 150 μm to allow cell colonization [1,6]. Still larger pore sizes and pore interconnections (> 300 μm) have been suggested to improve vascularization [7]. Therefore, scaffolds with a successful balance between the properties needed for adequate cellular function and viability and high mechanical strength remains challenging.

As signalled by Bohner [8], "a paradigm shift occurred at the turn of the millennium: instead of designing load-bearing bone graft substitutes, researchers aimed for bone graft substitutes providing a fast healing response, that is a fast turnover from a bone defect to mature (= mechanically competent) bone". In this sense, it has been proposed that a good balance between a high degree of porosity and mechanical properties comparable with cancellous bone should be sufficient for scaffold performance [9,10].

CPs are biocompatible, bioresorbable and bioactive compounds. In addition, as the solubility of CPs is pH dependent, their resorption is mostly controlled by their interaction with cells, which ensures concomitant material resorption and bone formation processes and the absence of biocompatibility issues due to the uncontrolled release of large amounts of degradation products [8,11,12]. Moreover, this pH dependent behaviour makes CaPs ideal encapsulating agents for drug and imaging agents because dissolution with release of the active agent would occur as pH decreases within the cell [11]. However, the extremely low toughness of CPs limits their application as sole constituents of scaffolds [3,8]. For example, maximum fracture toughness reported for HA bioceramics is 1.20 ± 0.05 MPa.m$^{1/2}$ [13].

Metals and polymers have been used to manufacture hybrid biomaterials trying to reach bone graft substitutes with high mechanical properties [4,5,8,14]. In particular, polymer-CPs composites, polymeric coatings on the CPs parts and infiltration of the porous structures by polymers have been proposed to overcome the lack of adequate mechanical behaviour of CPs. In general, the incorporation of polymers implies the decrease of final porosity of the scaffold which might lead to the decrease of properties such as bioactivity or osteoconductivity and/or inadequate resorption behaviour. Moreover, the release of large volumes of degradable polymers or metals might present biocompatibility problems.

The development of CPs-based ceramic-ceramic composites with improved mechanical behaviour might be a solution for inorganic scaffolds with sufficient mechanical properties and adequate biological response. Hydroxyapatite (HA) is the CaP with the best mechanical behaviour, however, it presents the lowest bioactivity - implants made of sintered HA are found in bone defects for many years after implantation [5]. The degradation rate of β-TCP is 3–12 times higher than that of HA [7]. A combination of titanium mesh with β-TCP granules and autologous human adipose-derived mesenchymal stem cells (hASCs) has been successfully applied in craniofacial surgery [15]. Future challenges include the displacement of the permanent Ti structure by a completely resorbable scaffold.

Wagoner Johnson et al [4] reviewed the mechanical behaviour of HA-β-TCP composites and the major conclusion was that β-TCP is detrimental to the mechanical behaviour. Most studies showed a continuous decrease of strength with increasing β-TCP and, in some cases, a peak in strength for low amount of second phase was found. It has been suggested that such behaviour would be caused by the introduction of microcracks during one or more phase transformations that can take place during sintering, however, this point has not been proven yet explicitly.

In order to understand the microstructures developed in β-TCP materials and their mechanical behaviour it is important to take into account the large crystalline thermal expansion anisotropy of this phase ($\alpha_{500-1000^{\circ}C}$: = 11.7 and 37.35 × 10^{-6} °C^{-1} for a and b axis, respectively, $\alpha_{average}$ = 20.2 × 10^{-6} °C^{-1}; calculated from Ref. [16]). When cooling β-TCP-containing materials from the sintering temperature, stresses are developed at the boundaries of grains with different orientations due to thermal expansion mismatch. Such stresses would remain as residual stresses in the sintered materials and/or lead to cracking for grain sizes larger than the critical one [17]. Therefore, microcracks and residual stresses that would add to the applied ones during use are expected in β –TCP containing materials. As a consequence, strength values reported for β –TCP materials are relatively low. For example, reported strength values determined using diametral compression of discs test, DCDT, are in the range 16–30 MPa –i.e: Characteristic strengths of sintered α + β-TCP [18] and β-TCP [19] materials are in the range of σ_0 = 16–20 MPa; average strength of a β-TCP sintered material is $\sigma_{av} \approx$ 19 MPa [19] and of a submicronic grain size β-TCP prepared by spark plasma sintering is σ_{av} = 28 ± 15 MPa [20] –.

Ceramic-ceramic composites with residual stresses and/or microcracks can be designed for improving specific properties. In this sense, materials developed in the pseudobinary system TCP-diopside present high potential. Apart from these biocompatible major phases, also wollastonite ($CaSiO_3$) is present in the system, which is highly bioactive. Diopside resorption is slower than that of β-TCP and presents much higher toughness ($K_{IC} \approx$ 3.5 and 1.1 MPa m$^{1/2}$ for diopside [21] and β-TCP [22], respectively), and stiffness ($E \approx$ 170 GPa and 110 GPa for diopside [21] and β-TCP [22].

In a previous work, it was hypothesized that a suitable microstructural design would allow to tailor the bioactivity and mechanical response of β-TCP-diopside composites [19]. Dense composites of β-$Ca_3(PO_4)_2$ with nominally 80 wt.% and 60 wt.% of $CaMg(SiO_3)_2$ processed by uniaxial pressing and sintering were developed. They presented higher tensile strength (> 3x) than TCP materials, for similar reliability, and supported viability and osteogenic differentiation of hASCs. The microstructure was constituted of highly microcracked β-TCP zones surrounded by uncracked and dense diopside. Initially, hASCs colonized the composites through the microcracked β-TCP phase which was preferentially resorbed leaving the structure of diopside. The specific biological behaviour permits to infer that in a composite-hASC scaffold, an initial bone structure would generate while maintaining the structural integrity of the remaining diopside which will be resorbed for longer times as the bone structure grows further.

In this work, we have investigated whether the improved mechanical behaviour due to the presence of diopside is maintained in highly porous scaffolds. The composition with 60 wt.% of diopside was chosen because of its higher bioactivity [19]. The microstructure of this material was constituted of highly microcracked β-TCP zones (largest dimension: 10–30 μm) surrounded by dense diopside. Fracture origins were the β-TCP areas and microcrack growth was limited by the tough diopside matrix which presented transgranular fracture. This fracture mode leads to strength values much higher than those for TCP materials (DCDT: σ_0 = 64 MPa, σ_{av} = 60 MPa).

Two kinds of model specimens with different levels and morphology of pores have been analysed. Freeze casting by ice templating has been used as processing route for obtaining the highly porous scaffolds. The technique consists on freezing a water slurry of ceramic particles, followed by ice removal by freeze drying. By applying a thermal gradient during the freezing, the ice crystal growth along this thermal gradient leads to an anisotropic porous structure after ice sublimation. Porosity in freeze cast materials has been demonstrated as adequate for the colonization by osteoblasts [23]. However, in order to promote the vascularization, pores need to be larger. For that reason, laser ablation of the green porous specimen has been carried out for obtaining larger cylindrical channels. The microstructure and mechanical behaviour of both kinds of specimens, freeze cast (FC) and freeze cast and laser ablated (FC + L), have been fully characterized and compared to those of

the dense composite previously reported.

2. Experimental

Diopside-β-tricalcium phosphate porous scaffolds with nominal composition 60 wt.% diopside + 40 wt.% TCP were prepared by solid state sintering of freeze cast specimens. The same starting materials - a high purity TCP commercial precursor (RPH tri-Calcium phosphate, Carlo Erba Reagents, Milano, Italy) and a synthesised diopside - and same relative proportions as in the previous work [19] were used. The average particle sizes of the powders were 1.6 μm and 5.7 μm, for diopside and the TCP precursor, respectively. Densities were 3.16 ± 0.04 g.cm^{-3} and 2.94 ± 0.03 g.cm^{-3}, for diopside and the TCP precursor, respectively.

For zeta potential determinations, diluted slurries were prepared in deionised water with 3.4 vol.%, 3.6 vol.% and 3.5 vol.% of solid contents for diopside, TCP precursor and the mixture, respectively). High solid content (30 vol.%) slurries were used for viscosity measurements and processing by freeze casting.

A commercial ammonium polymethacrylate anionic dispersant (Dolapix CE64, from Zschimmer and Schwarz, Germany) was used as dispersant agent. Zeta potential and particle size determinations (Acoustosizer IIS, Colloidal dynamics, Australia) were used for determining the optimal amount of dispersant to reach stable suspensions. Slurries for the single ceramic powders -diopside and the TCP precursor- and for the mixture of 60 wt.% diopside + 40 wt.% TCP were characterized. The three slurries have been titrated with 10 wt.% of the commercial dispersant agent.

The rheological characterization was done with a cone/plane geometry rheometer of 1° and 60 mm diameter (Haake RS150, ThermoHaake, Germany) suitable for measuring an extended viscosity range. The slip was deposited in the space between the two supports and the measurements were done for a shear rate varying from 0 to 1000 s^{-1}. Slurries with 2.5, 3.0 and 3.5 wt.% dispersant were prepared in order to determine the optimal dispersing condition of the slurry containing the mixture of diopside and TCP precursor.

For freeze casting, 2 ml of slurry was poured into a cylindrical TEFLON mould with 3 holes of 17 mm for inner diameter and 50 mm height, and put on the freezing device. Two freezing rates, low and high, were used to check their influence on the characteristics of the obtained structure. For the low freezing rate, the sample holder was cooled at 1 °C/min down to 40 °C, and then the temperature was kept constant until the full freezing of the slurry was achieved. For the high freezing rate, liquid nitrogen was used for cooling the sample holder; no control of the temperatures involved was performed; the freezing rate can be estimated as 20 °C/min [24]. The frozen samples were then placed in a freeze dryer (HETO CD8, Thermo Fisher Scientific, USA) for 48 h to remove the solvent at a pressure close to 10 Pa. Before sintering, the freeze cast specimens were cylinders of diameter ≈ 17 mm and height ≈ 9 mm.

Sintering was performed at 1225 °C during 2 h and using 10 °C/min as heating and cooling rates, according to the optimized schedule previously established [19]. The dimensions of the specimens after sintering were diameter ≈ 13 mm and height ≈ 7 mm.

The bulk density and the open porosity of sintered specimens were determined following the standard EN1389:2003. Reported values are the average of four determinations and errors are the standard deviations.

The microstructural characterization of the sintered freeze cast specimens (low and high freezing rates) was done by scanning electron microscopy (SEM, HITACHI S-3500 N and JEOL JSM 5900 L V, Japan). Half specimens cut parallel to the freezing direction (transversal specimens) with a diamond disc as well as the top surfaces (perpendicular to the freezing direction) of specimens were analysed. Surfaces were hand polished up to a grit size of P2000 and coated with gold. Texture was observed in the transversal specimens and the top surfaces were used to measure the pore size. The elliptical pore shape was characterized by the average values of the minor and major axes. 5 micrographs with more than 100 pores in total were investigated for each freezing condition using MESURIM software (ACCES, France).

Mechanical characterization of the sintered specimens was performed, as in the previous work [19], in terms of the diametral compression strength using stainless steel plates and a paperboard between the plates and the specimens. A universal testing machine (Microtest, Spain) and a rate of displacement of the machine frame of 0.5 mm/min were used.

The strength was calculated according to (Eq. (1) [25]):

$$\sigma_f = \frac{2F}{\pi D t} \quad (1)$$

Strength results for each condition, i.e. high and low cooling rate, are given as the average of four determinations and error as the standard deviations.

Specimens processed using the high rate were selected for laser ablation (Trumpark Station 5000, Trumpf, Germany). The processing parameters are a q-switch mode with a spot size of 40 μm, a hatch of 60 μm, power of 20 W and a scan speed of 2000 mm·s^{-1}. With this parameter, cylindrical holes were created at the top surface of the green specimens with diameter of 800 μm and a depth of about 2 mm. The final diameters of the channels after sintering were ≈ 700 μm.

Fig. 1 shows the schematics of the freeze cast and sintered specimens with the laser ablated channels. Two discs were machined from the freeze cast part (labelled as FC)and one disc from the freeze cast part containing laser ablated channels (labelled as FC + L), Fig. 1a. The disc specimens (heigth ≈ 2 mm) were tested in diametral compression as described above. For testing, the FC + L specimens were positioned in such a way that the lines formed by the round sections of the laser channels in the specimen cross sections were parallel and perpendicular to the load (Fig. 1 b).

X-ray diffraction (XRD, D8 Advance, Bruker AXS GmbH, Germany) was performed with copper anode ($CuK_\alpha 1$ λ = 0.15418 nm) working at 40 kV and 40 mA. Determinations were done on samples rotating at 15 rpm. in the interval 2–90 º (2θ) and X-ray patterns were acquired with a step of 0.03° and counting time of 2.5 s. Powders milled from the FC and FC + L discs were characterized. In addition, XRD analysis of a powder sample of a dense specimen previously developed [19] was performed using the same conditions. Identification of the crystalline phases was done using the PDF files #9–169, #11–654 and # 84–0655, for β-TCP, diopside and the low temperature wollastonite polymorph (W-2 M), respectively.

Semiquantitative analysis of the phase fractions was performed using EVA software (EVA V5.0, Bruker AXS GmbH, Germany). Major and not convolved diffraction peaks at 2theta angles of 56.4°, 53.3° and 28.8° for diopside, β-TCP and wollastonite, respectively, were used.

For detailed microstructural analysis, cross sections of the specimens (perpendicular to the freezing direction) were embedded in a resin and diamond polished (down to 1 μm). A light chemical etching with 5% HF solution for 15 s was done to reveal the microstructure. The surfaces were coated with Au and characterized by scanning electron microscope (SEM; Tabletop Microscope TM-1000, Hitachi, Japan) and field emission scanning electron microscopy with X-ray energy-dispersive, EDS spectrometry (EDS-FE-SEM, S-4700, Hitachi, Japan). Au-coated fracture surfaces were also observed and analysed by EDS-FE-SEM to identify the phases by their constituents (wollastonite Si + Ca; diopside: P + Si + Ca + Mg; β-TCP: P + Ca). It is important to remark that relative intensities of the peaks cannot be used as indicators of the composition because the emission of the Au coating, necessary for well-defined surfaces, interacts with that of P.

For the statistical analysis of strength data, results of sixteen valid tests were used to calculate the Weibull parameters and their upper and lower 90% confidence limits using the procedure of ENV-843-5.

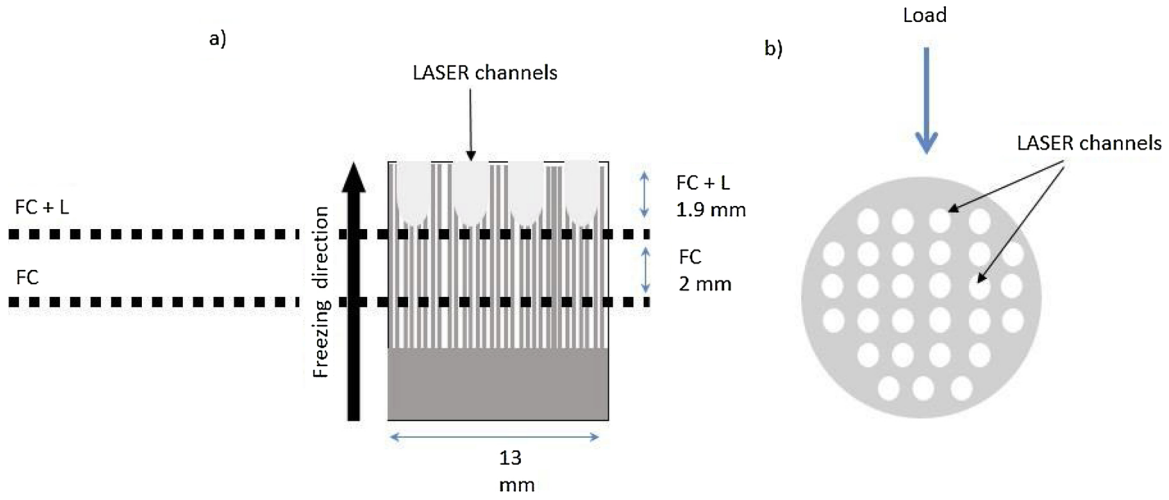

Fig. 1. Schema of the freeze cast and sintered specimens with the laser channels.
(a)Transversal section showing the zones of extraction of the discs for testing, FC and FC + L, and the surfaces polished for FE-SEM observation (dotted lines).
(b) Cross section showing the direction of applied load for DCDT.

3. Results

Zeta potential values as a function of the amount of dispersing agent are plotted in Fig. 2. When no dispersing agent is added, the starting pH is around 5.5 and the zeta potential is positive (≈ 2.5 mV) for the TCP precursor. The starting pH for diopside is higher (≈ 11) and the zeta potential is negative (≈– 21 mV). Adding dispersant up to 5 wt.% leads to a decrease of zeta potential down to around −20 mV and −30 mV for the TCP precursor and diopside, respectively. For the mixture of TCP precursor and diopside the starting pH is 10.7 with a zeta potential of −13 mV. Increasing the dispersant amount leads to a decrease of zeta potential of slurry down to ≈ -25 mV, which is considered to be low enough for having a good stability when this dispersing agent is used (−20 mV) [26].

From the zeta potential measurements, 5 wt.% addition of dispersant would be adequate for stabilisation of the mixture slurry. However, such amount is relatively high so it was necessary to analyse other slurry parameters. It is well known that a minimum in the viscosity of ceramic slurry is reached at the best de-agglomeration point [27], therefore, the viscosity was measured as a function of the dispersing agent content to check whether lower amounts would provide adequate low viscosity. As shown in Fig. 3, minimum viscosity was reached for a dispersing agent content of 3 wt.% and, moreover, the reached viscosity (≈ 35 mPa·s) was adequate for pouring the slurry into the moulds to perform freeze casting. Therefore, 3 wt.% of dispersant was selected for the fabrication of the specimens.

Figs. 4 and 5 show characteristic transversal sections of sintered specimens prepared at low and high freezing rates. Both structures are the classic anisotropic ones obtained by freeze casting. At the bottom of the specimens (zone A) relatively dense zones with heterogeneous microstructure are observed, the heights of these zone were 1.7 mm and 0.4 mm for the low and high freezing rates, respectively. The remaining of the specimens (zone B) was formed by elongated pores with elliptical cross sections (zone C) which dimensions were much larger for the specimens fabricated using the low cooling rate (Table 1).

Density and porosity values for the sintered specimens are summarized in Table 2. For the specimens processed using the low rate, density is slightly lower (≈ 10%) and open porosity is slightly higher (≈10%) than for the specimens processed using the high cooling rate.

Average strength values for the sintered cylinders processed by freeze casting were 1.7 ± 0.3 MPa and 3.8 ± 0.3 MPa, for the specimens fabricated using the low and high speeds, respectively.

The XRD diffractograms of the machined discs are plotted in Fig. 6 together with the corresponding reference material from previous study [19]. They are similar for the three kinds of specimens. Two major phases, β-$Ca_3(PO_4)_2$ and $CaMg(SiO_3)_2$ and the low polymorph of

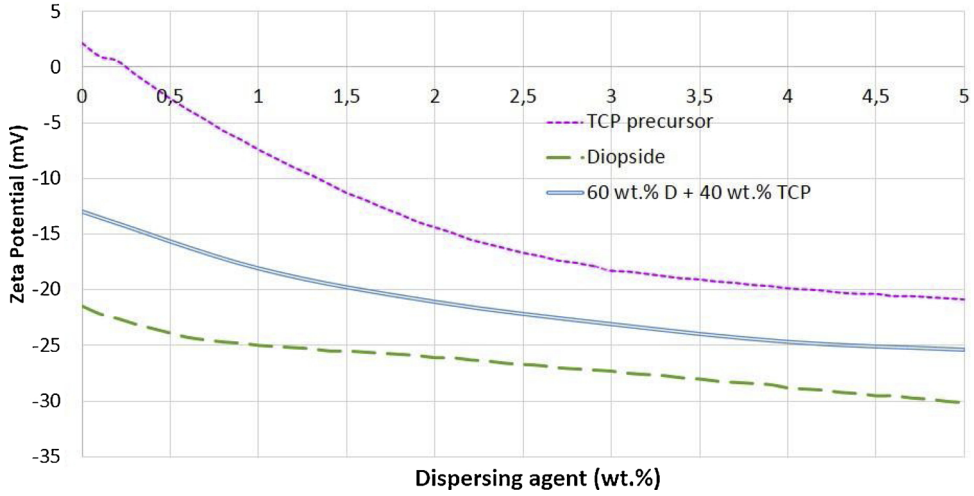

Fig. 2. Zeta potential versus the amount of dispersing agent (Dolapix CE64) added to slurries of the indicated powders.

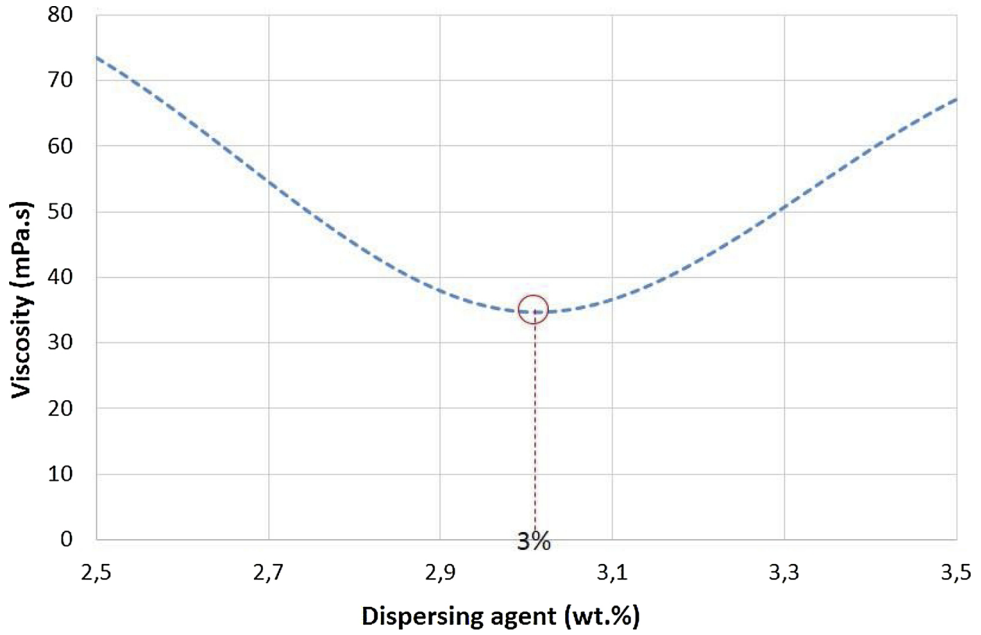

Fig. 3. Effect of the concentration of dispersing agent (Dolapix CE64) on the viscosity of the slurry with 30 vol.% solid loading of the mixture diopside + TCP precursor.

$CaSiO_3$, W-2 M, as minor phase were identified. Semi-quantitative analysis gave a crystalline phase composition of ≈ 60 wt.%, 34 wt.% and 6 wt.% for diopside, β-TCP and wollastonite, respectively. The calculated oxide contents corresponding to these crystalline phase fractions (38, 20, 10 and 32 wt.% for CaO, P_2O_5, MgO and SiO_2, respectively) are fairly coincident with those chemically analysed in the studied composition (36.6, 19.0, 10.6 and 33.7 wt.% for CaO, P_2O_5, MgO and SiO_2, respectively), which supports the quality of the semi-quantitative evaluations.

The Weibull parameters calculated from the experimental strength data for the machined discs are summarized in Table 3. There are no significant differences between the values of the Weibull modulus while the characteristic strength of the specimen FC + L is lower by 38% compared to FC samples.

The main microstructural features found in the machined discs are summarized in Figs. 7–11. The cross section of all specimens showed the elliptical sections of the elongated pores formed by freeze casting, surrounded by the ceramic composite (Fig. 7 a–b) and the rounded sections of the laser channels in specimens FC + L. The same microstructural features were found in both kinds of specimens, FC and FC + L, even close to the laser channels in the later ones.

The ceramic composite microstructure (Figs. 7c and 8) was constituted by a substructure made of small particles (< 10 μm) and dense zones of larger dimensions (largest dimension up to 40 μm). This

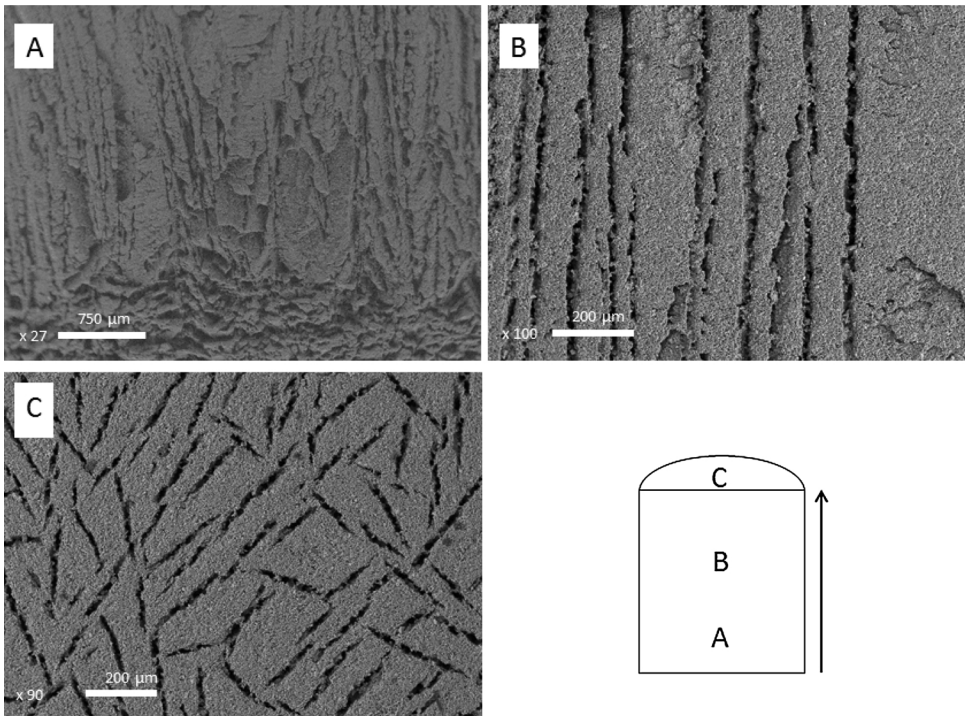

Fig. 4. Characteristic features found in sintered composite specimens prepared using the low freezing rate. As shown in the schema, zones A and B are found in the transversal sections while zone C corresponds to the top surface. In the transversal sections, heterogeneous zones are observed at the bottom (A) and the elongated pore channels in the middle (B). The elliptic pore shape is observed in the cross section of the top surface (C). SEM micrographs.

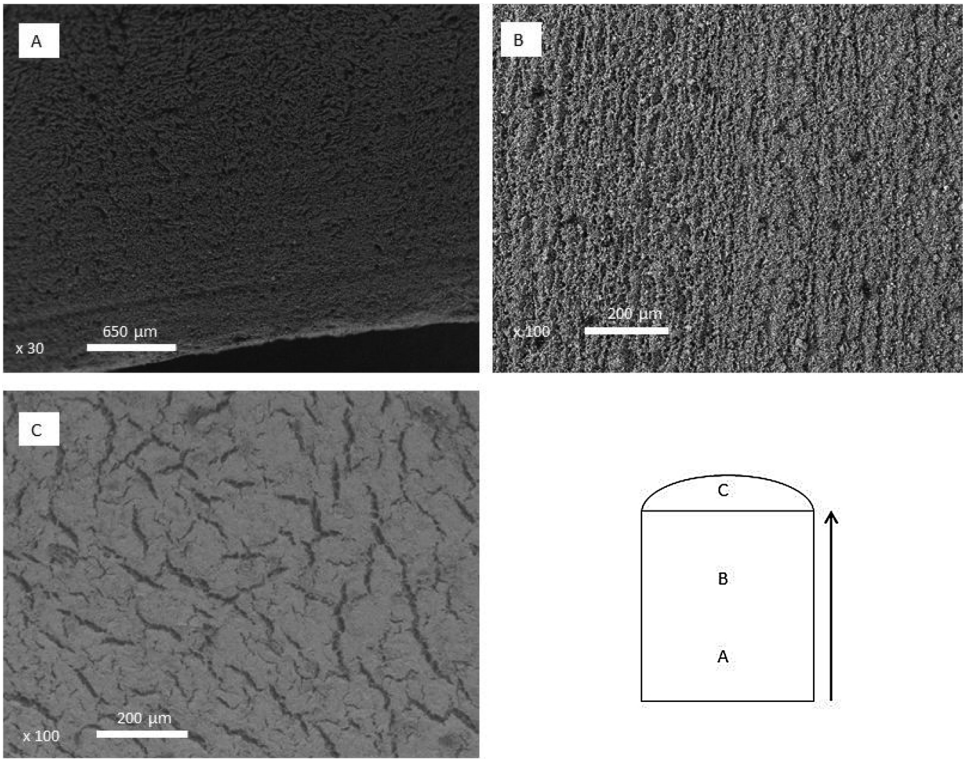

Fig. 5. Characteristic features found in sintered composite specimens prepared using the high freezing rate. As shown in the schema, zones A and B are found in the transversal sections while zone C corresponds to the top surface. In the transversal sections, heterogeneous zones are observed at the bottom (A) and the elongated pore channels in the middle (B). The elliptic pore shape is observed in the cross section of the top surface (C). SEM micrographs.

Table 1
Dimension of the cross sections of the pores in the sintered freeze cast specimens.

	Freezing rate (ºC/min)	
	−1 (Low)	−20 (High)
Major axis (µm)	160 ± 65	66 ± 30
Minor axis (µm)	20 ± 3	14 ± 3

Table 2
Density and porosity values for the sintered freeze cast specimens.

	Freezing rate (ºC/min)	
	1 (Low)	≈ 20 (High)
Bulk density (g/cm^3)	1.44 ± 0.02	1.62 ± 0.02
Open porosity (%)	0.54 ± 0.01	0.49 ± 0.01
Relative density (% of T.D)	46.7 ± 0.7	52.6 ± 0.6

microstructure was more open in zones close to the laser channels, which had very irregular boundaries (Figs. 7b and 8 b).

As observed in the low magnification micrographs of the central part of the specimens, no singular defects origin of the fracture (i.e. critical defects) were observed in any fracture surface (Fig. 9 a,b) and the structure of elongated pores characteristic of freeze casting was revealed by fracture (Fig. 9 c,d). The laser channels with a conical shape were observed in the FC + L specimens (Fig. 9 b).

EDS analyses allowed the identification of the phases detected by XRD (Fig. 6). The denser zones observed in the polished specimens were submatrices of β-TCP particles with rounded surfaces surrounded by pores, diopside and some wollastonite particles (Fig. 10). These later two phases presented transgranular fracture (Figs. 10 and 11 a,b). In general, the β-TCP submatrices were not microcracked (Figs. 10 and 11b); only the largest agglomerates of β-TCP with the maximum dimensions of 40 µm were microcracked.

4. Discussion

The above described results demonstrate that it is possible to fabricate freeze cast specimens using the composition 60 wt.% diopside-40 wt.% TCP previously reported [19]. For both freezing rates used, the sintered specimens present the characteristic texture formed by aligned elongated pores of elliptical cross section (Figs. 4 and 5) reported elsewhere [28]. The observed denser zones form due to the relatively high freezing rate at the beginning of the freezing process.

It has been reported [29] that the size of the pores decreases as the freezing rate increases, as observed in this work (Table 1). High freezing rates lead to the formation of a higher number of ice nuclei and then, more small ice crystals become pores after ice sublimation. The ice crystals are allowed to grow when low freezing rates are used, leading to bigger pores.

In principle, the porosity level is determined by the solid content in the slurries [30], which was the same for both freezing rates. However, the more stable growth associated to the low rate permits the development of a slightly higher proportion of open channels, as revealed by the lower density and higher porosity of the specimens processed using this rate (Table 2).

The fact that the porous texture is revealed in the fracture surfaces indicates that fracture occurs by the coalescence of the channels and, in fact, strength of the specimens fabricated using the low rate is the lowest.

The pore sizes of the specimens fabricated using the high freezing rate (Table 2) are much larger (≈ 5x) than those found using the same rate in a previous work [23] devoted to freeze casting of single phase β-TCP (≈ 6 µm and 13 µm for the minor and major axis, respectively) which demonstrates the extreme dependence of texture formed by freeze casting on powder characteristics.

The high freezing rate was chosen for further material processing because the low rate gave specimens with extremely low strengths. Moreover, in the above-mentioned work it was demonstrated that major axes around 100 µm were sufficient for the pores to be colonized by osteoblasts.

Both kinds of disc specimens, FC and FC + L, presented the same

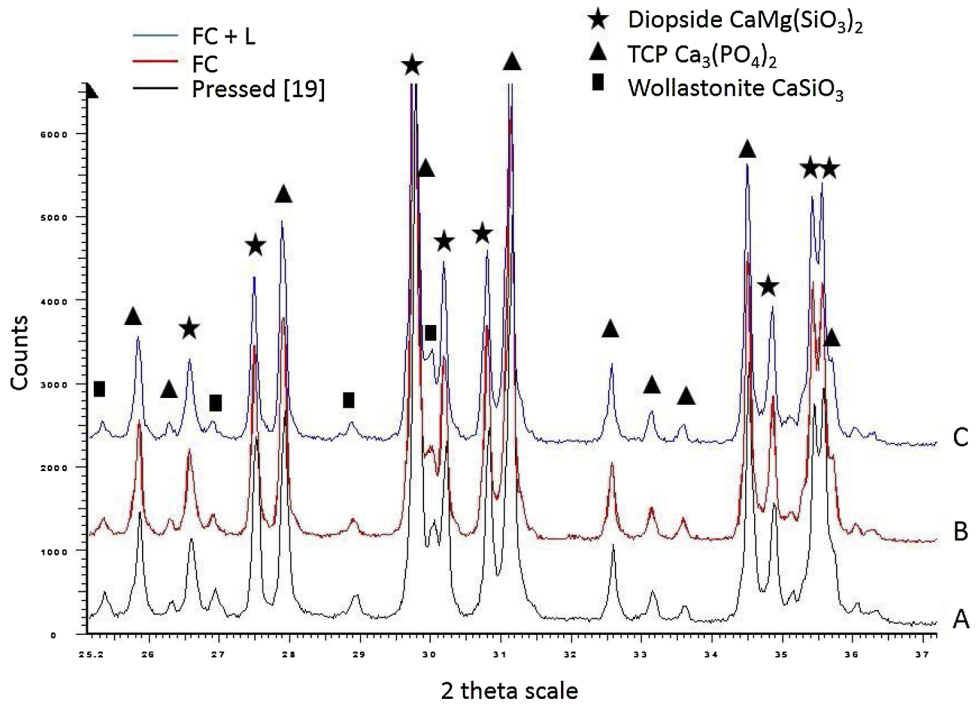

Fig. 6. XRD diffraction patterns of the sintered specimens. A: specimen prepared by pressing used as reference [19]. B and C: machined specimens (see Fig. 1) from the freeze cast (FC) and freeze cast and laser zones (FC + L), respectively.

Table 3
Weibull parameters calculated for 90% of confidence limits. Disc specimens machined from the sintered freeze cast and laser ablated cylinders. FC: zone without laser channels; FC + L: zone with laser channels. Weibull modulus, m, and its upper, D_u, and lower limits, D_l; characteristic strength, σ_0, and its upper, C_u, and lower, C_l, limits. For the reference dense specimens from Ref. [19] experimental values and those corrected using the Weibull relationship (Eq. (3)) are included.

	m	D_u	D_l	σ_0 (MPa)	C_u (MPa)	C_l (MPa)
FC	5.7	7.3	3.7	4.0	4.3	3.7
FC + L	6.4	8.3	4.2	2.5	2.7	2.3
Dense	6.1	8	4	64	70	60
Dense corrected	–	–	–	57	63	54

crystalline phase composition and microstructural features (Figs. 7–11). These facts mean that, in spite of the high and uncontrolled temperature involved in the process of ablation, it does not severely affect the microstructure of the materials. Therefore, laser ablation appears as an adequate method for introducing relatively large channels in bioceramic scaffolds to allow vascularization.

The phase content as well as the general aspects of the microstructure, i.e. β-TCP submatrices surrounded by diopside, are in good agreement with those in the dense specimens previously developed [19], which would indicate that the new processing route followed in this work respects the main aspects that were sought in the microstructure. The rounded shape of β-TCP particles reveals their growth in contact with vapour. The β-TCP submatrices in the material developed here do not present extensive microcracking as occurred in the previous material because they grow surrounded, not only by the high stiffness diopside but also by pores that will allow thermal strain accommodation during cooling. Therefore, the critical size for spontaneous microcracking is increased and only the largest agglomerates present microcracks (Fig. 11c).

Weibull modulus are similar to the value determined for the reference dense composite (m = 6.1 [19]), which means that reliability is maintained in the developed scaffolds.

The aspect of the fracture surfaces, in which the structure of the elongated pores formed during freeze casting is revealed (Fig. 9), indicates that failure occurs by the coalescence of such pores. Cracks have to traverse the composite structure for the pore coalescence to occur.

To analyse the effect of the porous structure on strength and to discern whether the composite microstructure in the developed scaffolds plays a similar role as that observed in the dense specimens, the deleterious effect of porosity on strength has been evaluated as described below.

In order to compare the strength values of the scaffolds developed in this work with those of the dense specimens, it is necessary to correct the values taking into account the different effective volumes associated to the different sizes of the discs used for testing (radius ≈ 4 mm and 6.5 mm for the dense and FC discs, respectively; and thickness ≈ 3 mm and 2 mm for the dense and FC discs, respectively).

The stressed volumes, V, in DCDT specimens are given by (Eq. (2)) [25]:

$$V \approx R^2\, t/5 \tag{2}$$

where, R and t are the radius and the thickness of the specimen, respectively.

Considering the Weibull relationship between the strength values and the effective volumes (Eq. (3)):

$$(V_1/V_2)^{1/m} = \sigma_2/\sigma_1 \tag{3}$$

The expected strength values for dense specimens of the same sizes as the specimens tested in this work, $\sigma_{corrected}$, is:

$$\sigma_{\text{corrected}} = 0.9\ \sigma_{\text{d}}$$

where, σ_d, are the experimental values determined previously [19].

The corrected value for the characteristic strength of the dense

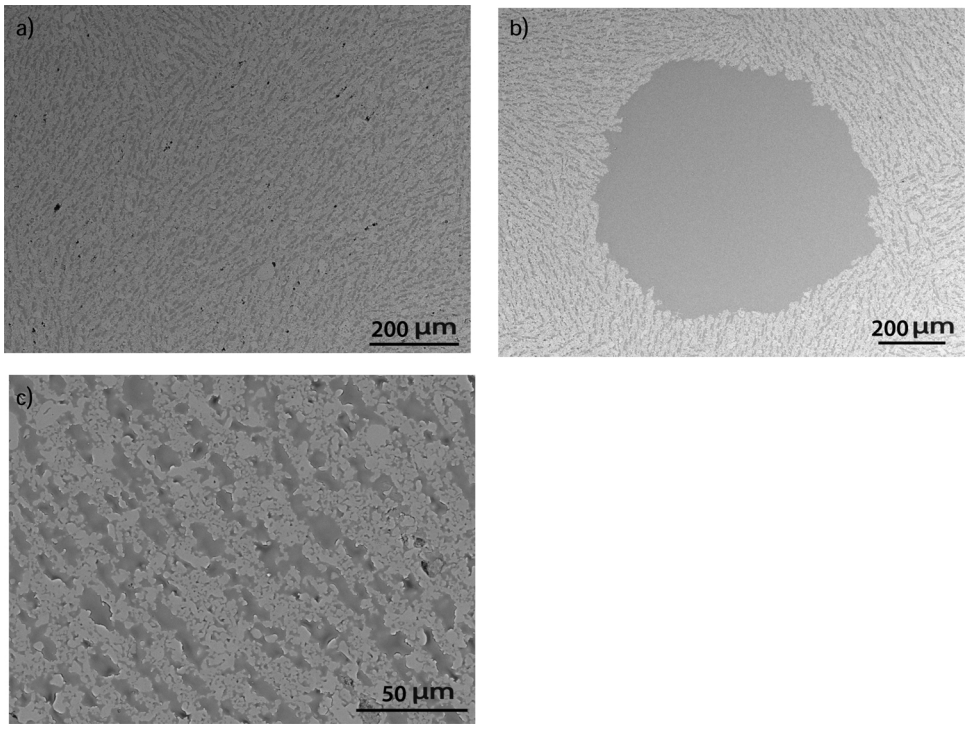

Fig. 7. Characteristic features observed in the cross sections of the disc specimens. SEM of polished and chemically etched surfaces. Light gray is the ceramic material, dark gray are the pores filled by resin and black are the pores non filled by resin.
(a) Low magnification micrograph showing the elongated pores surrounded by the ceramic composite. FC specimen.
(b) Low magnification micrograph showing the elongated pores surrounded by the ceramic composite and a laser channel. FC + L specimen.
(c) Higher magnification micrograph showing details of the microstructure of the composite and the pores (see Fig. 8). FC + L specimen.

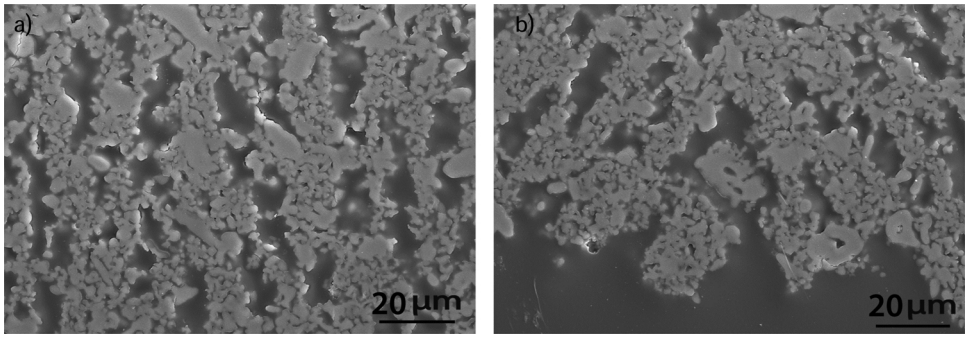

Fig. 8. Characteristic features observed in the cross sections of the disc specimens. FE-SEM of polished and chemically etched surfaces. Light gray is the ceramic material and dark gray are the pores filled by resin.
Details of the microstructure: elliptical shaped pores surrounded by the composite. The composite presents a substructure made of small particles ≈ µm and dense zones of larger dimensions (largest dimension ≈ 10 µm).
(a) FC + L specimen, zone between the laser channels.
(b) FC + L specimen, boundary of a laser channel.

specimens, included in Table 3, is about one order of magnitude higher than that of the FC specimens.

For a material with the same porosity level as the FC specimens, closed spherical pores and pore walls constituted by the dense composite it is possible to calculate the expected strength, σ, by applying the minimum solid area model [31]

$$\sigma = \sigma_0 \exp(-3P) \quad (4)$$

where σ_0 is the strength of the materials without porosity, (57 MPa, Table 3), and P is the porosity, 0.5 (Table 2). The calculated strength value, 13 MPa, is about 3 times higher than that of obtained for the porous scaffolds. Such discrepancy is due to the specific open pore geometry developed by freeze casting. To evaluate the expected strength for the freeze cast scaffolds, the simplified model of a bidimensional cellular porous microstructure uniaxially loaded has been considered [32]. The relationship between the strength for brittle crushing of the structure, σ_{sc}, and that of the walls, σ_W, is given by (Eq. (5)):

$$\sigma_{sc} / \sigma_W = 0.2 (\rho_{sc} / \rho_W)^{3/2} \quad (5)$$

where ρ_{sc} and ρ_W are the densities of the scaffold and the walls, respectively.

Considering the density value for de FC specimens (Table 2) and that of the dense material (2.98 g/cm^3 [19]), the expected relationship will be (Eq. (6)):

$$\sigma_{sc} = 0.084\ \sigma_W \quad (6)$$

Taking for σ_W the corrected value for the dense specimens, Eq. (6) gives for the scaffold a strength of 4.7 MPa, a value close to the characteristic strength of the FC specimens (Table 3).

The toughness of the composite microstructure developed in the freeze cast cylinders during fracture is similar to that of the dense materials. This fact is due to the effect of diopside, which presents transgranular fracture hindering the crack propagation from the β-TCP areas and the pores (Figs. 10 and 11) as occurred in the dense specimens.

The strength of the specimens (FC + L) is further decreased by the large pore channels introduced by laser ablation. However, values are in the range of those of tensile strength of fresh cancellous bone of different origins, 0.3–20 MPa [33]. As discussed in the introduction it

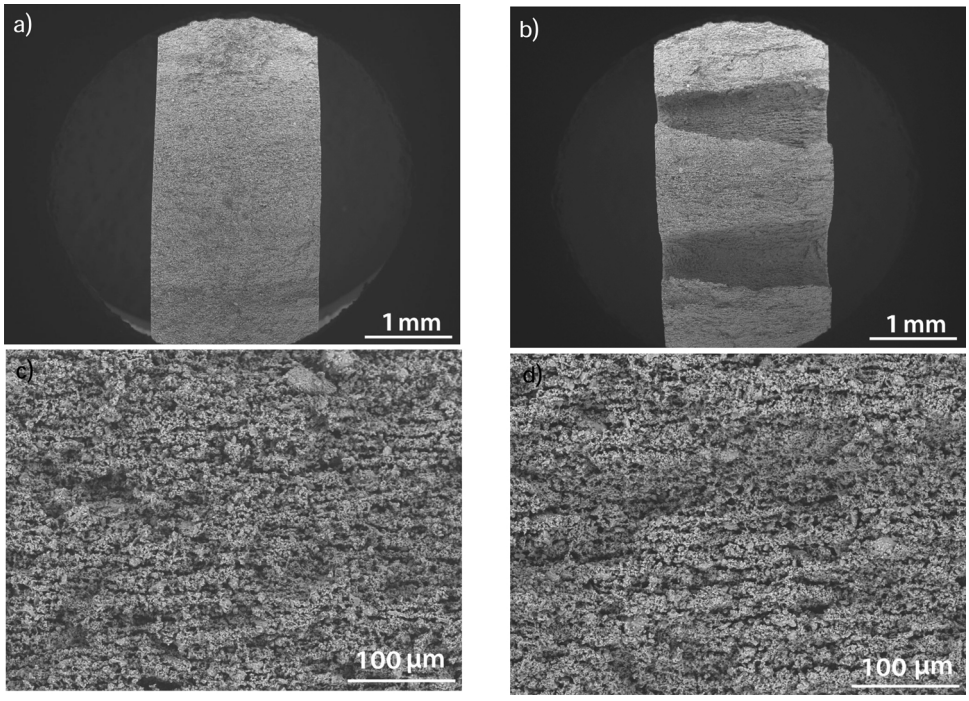

Fig. 9. Characteristic features found in the fracture surfaces. SEM. No singular defects are observed at low magnification (a, b) and the structure formed by elongated pores is observed (c, d). (a) FC specimen. (b) FC + L specimen. The laser channels with conical shape are shown. (c) FC specimen. (d) FC + L specimen.

has been proposed that a good balance between a high degree of porosity and mechanical properties comparable with cancellous bone should be sufficient for scaffold performance [9,10]. Therefore, results from this work demonstrate that scaffolds with large pores constituted by the composite material proposed will be adequate for bone regeneration. In particular, these scaffolds would provide sufficient initial mechanical strength and stiffness to keep the shape of plate bones, such as craniofacial. In addition, the differential resorption rate of diopside [19] will permit cell seeding of the scaffold in vitro without compromising scaffold architecture.

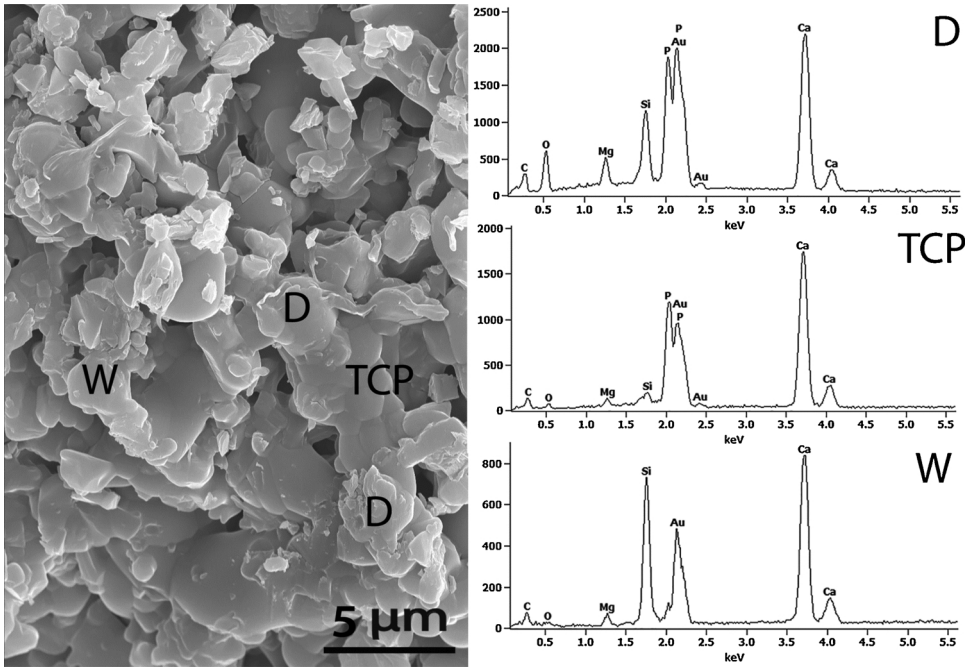

Fig. 10. Identification of the constituents of the ceramic composite in FC and FC + L materials. FE-SEM and EDS analyses. Submatrices of β-TCP grains with rounded surfaces and pores surrounded by diopside (D) and some wollastonite (W). Specimen FC.

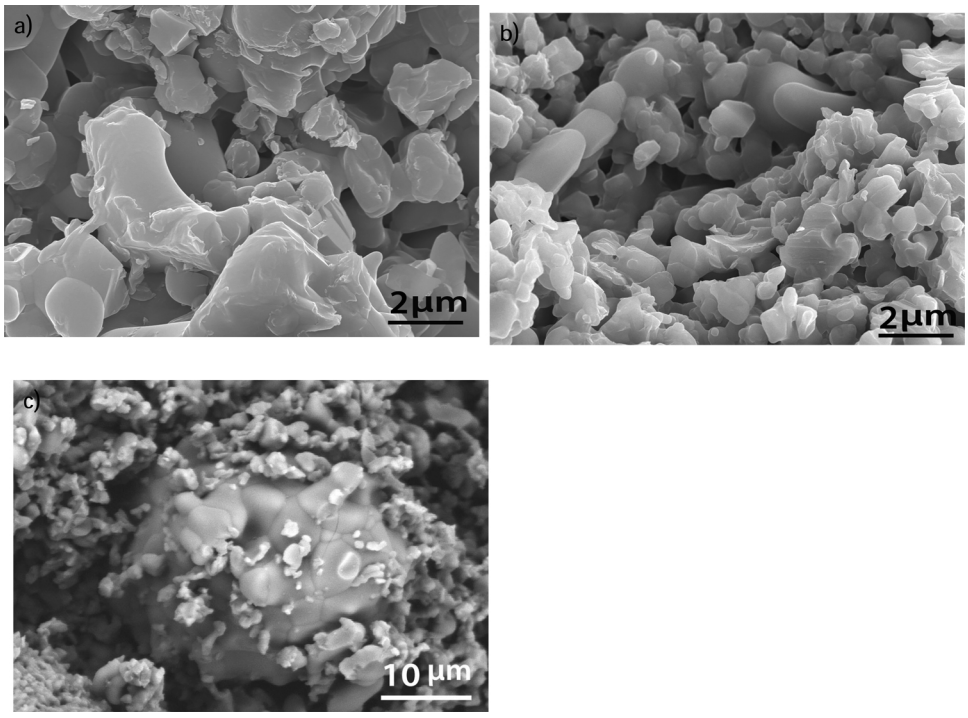

Fig. 11. Details of the fracture mode in FC and FC + L specimens. (a) Diopside with transgranular fracture surrounding pores. FE-SEM. FC specimen. (b) Diopside with transgranular fracture surrounding β-TCP grains with rounded boundaries. FE-SEM. FC + L specimen. (c) β-TCP agglomerate with microcracks. SEM. FC specimen.

5. Conclusions

It is possible to fabricate porous scaffolds of $CaMg(SiO_3)_2$ - β-$Ca_3(PO_4)_2$ composite ceramic using freeze casting and laser ablation. The crystalline phases present in the sintered specimens are the same as those found in dense composites shaped by uniaxial pressing.

The composites have dense walls surrounding elongated pores with elliptical cross sections with major axes up to 100 µm and channels with circular cross section of diameter around 700 µm. The bimodal pore distribution will allow adequate cell colonization and vascularisation.

The improved mechanical behaviour due to the presence of $CaMg(SiO_3)_2$ is maintained in the porous materials in which this phase keeps its transgranular fracture mode. Strength values of the porous scaffold developed are in the range of those of cancellous bone.

These results open the possibility of developing resorbable scaffolds for bone regeneration with high porosity and walls constituted by $CaMg(SiO_3)_2$ - β-$Ca_3(PO_4)_2$ composite.

Declaration of interests

The authors declare that they have no known competing financial interests or personal relationships that could have appeared to influence the work reported in this paper.

Acknowledgements

Work was performed in the frame of COST Action MP1301, NEWGEN, and project CSIC PIE 201660E097 (Spain).

References

[1] G. Turnbull, J. Clarke, F. Picard, P. Riches, L. Jia, F. Han, B. Li, W. Shu, 3D bioactive composite scaffolds for bone tissue engineering, Bioact. Mater. 3 (2018) 278–314, https://doi.org/10.1016/j.bioactmat.2017.10.001.
[2] F. Albee, H. Morrison, Studies in bone growth, Ann. Surg. 71 (1920) 32–38.
[3] S.V. Dorozhkin, Bioceramics of calcium orthophosphates, Biomaterials 31 (7) (2010) 1465–1485, https://doi.org/10.1016/j.biomaterials.2009.11.050.
[4] A.J. Wagoner Johnson, B.A. Herschler, A review of the mechanical behavior of CaP and CaP/polymer composites for applications in bone replacement and repair, Acta Biomater. 7 (1) (2011) 16–30, https://doi.org/10.1016/j.actbio.2010.07.012.
[5] S.V. Dorozhkin, Calcium orthophosphate (CaPO4) scaffolds for bone tissue engineering applications, J. Biotechnol. Biomed. Sci. 1 (3) (2018) 1–25, https://doi.org/10.14302/issn.2576-6694.jbbs-18-2143.
[6] M. Bohner, L. Galea, N. Doebelin, Calcium phosphate bone graft substitutes: failures and hopes, J. Eur. Ceram. Soc. 32 (2012) 2663–2671, https://doi.org/10.1016/j.jeurceramsoc.2012.02.028.
[7] D.W. Hutmacher, J.T. Schantz, C.X. Lam, K.C. Tan, T.C. Lim, State of the art and future directions of scaffold-based bone engineering from a biomaterials perspective, J. Tissue Eng. Regen. M 1 (2007) 245–260, https://doi.org/10.1002/term.24.
[8] W. Habraken, P. Habibovic, M. Epple, M. Bohner, Calcium phosphates in biomedical applications: materials for the future? Mater. Today 19 (2) (2016) 69–87, https://doi.org/10.1016/j.mattod.2015.10.008.
[9] T. Kokubo, H.-M. Kim, M. Kawashita, Novel bioactive materials with different mechanical properties, Biomaterials 24 (2003) 2161–2175, https://doi.org/10.1016/S0142-9612(03)00044-9.
[10] I.D. Thompson, L.L. Hench, Mechanical properties of bioactive glasses, glass-ceramics and composites, Proc. Inst. Mech. Eng. H 212 (2) (1998) 127–136, https://doi.org/10.1243/0954411981533908.
[11] O.A. Pinto, A. Tabaković, T.M. Goff, Y. Liu, and J.H. Adair, Calcium phosphate and calcium phosphosilicate mediated drug delivery and imaging, intracellular delivery: fundamentals and applications, fundamental biomedical technologies 5, A. Prokop 713-744. https://doi/10.1007/978-94-007-1248-5_23.
[12] L.C. Chow, Development of self-Setting calcium phosphate cements, J. Ceram. Soc. Jpn 99 (10) (1991) 954–964, https://doi.org/10.2109/jcersj.99.954.
[13] R. Halouani, D. Bernache-Assolant, E. Champion, A. Ababou, Microstructure and related mechanical properties of hot pressed hydroxyapatite ceramics, J. Mater. Sci. Mater. Med. 5 (1994) 563–568, https://doi.org/10.1007/BF00124890.
[14] A.V. Do, B. Khorsand, S.M. Geary, A.K. Salem, 3D Printing of scaffolds for tissue regeneration applications, Adv. Healthc. Mater. 4 (2015) 1742–1762, https://doi.org/10.1002/adhm.201500168.
[15] G.K. Sándor, V.J. Tuovinen, J. Wolff, M. Patrikoski, J. Jokinen, E. Nieminen, B. Mannerström, O.-P. Lappalainen, R. Seppänen, S. Miettinen, Adipose stem cell tissue-engineered construct used to treat large anterior mandibular defect: a case report and review of the clinical application of good manufacturing practice-level adipose stem cells for bone regeneration, J. Oral Maxillofac. Surg. 71 (5) (2013) 938–950, https://doi.org/10.1016/j.joms.2012.11.014.
[16] S. Nakamura, R. Otsuka, H. Aoki, M. Akao, N. Miura, T. Yamamoto, Thermal expansion of hydroxyapatite-β-tricalcium phosphate ceramics, Thermochim. Acta 165 (1990) 57–72, https://doi.org/10.1016/0040-6031(90)80206-E.
[17] E.D. Case, J.R. Smyth, O. Hunter, Grain-size dependence of microcrack initiation in brittle materials, J. Mater. Sci. 15 (1980) 149–153, https://doi.org/10.1007/BF00552439.
[18] I.H. García-Páez, R. García-Carrodeguas, A.H. De Aza, C. Baudín, P. Pena, Effect of Mg and Si co-substitution on microstructure and strength of tricalcium phosphate ceramics, J. Mech. Behav. Biomed. Mater. 30 (2014) 1–15, https://doi.org/10.1016/j.jmbbm.2013.10.011.
[19] S. Vanhatupa, S. Miettinen, P. Pena, C. Baudín, Diopside-tricalcium phosphate bioactive ceramics for osteogenic differentiation of human adipose stem cells, J. Biomed. Mater. Res. (2019) 1–15 doi.org/10.1002/jbm.b.34436.
[20] S. Tkachenko, M. Horynová, M. Casas-Luna, S. Diaz-de-la-Torre, K. Dvorak, L. Celko, J.M. Kaiser, E.B. Montufar, Strength and fracture mechanism of iron

reinforced tricalcium phosphate cermet fabricated by spark plasma sintering, J. Mech. Behav. Biomed. Mater. 81 (2018) 16–25, https://doi.org/10.1016/j.jmbbm.2018.02.016.
[21] T. Nonami, S. Tsutsumi, Study of diopside ceramics for biomaterials, J. Mater. Sci. Mater. Med. 10 (18) (1999) 475–479, https://doi.org/10.1023/A:1008996908797.
[22] A. Garcia-Prieto, J.C. Hornez, A. Leriche, P. Pena, C. Baudin, Influence of porosity on the mechanical behaviour of single phase β-TCP ceramics, Ceram. Int. 43 (2017) 6048–6053, https://doi.org/10.1016/j.ceramint.2017.01.146.
[23] E. Meurice, F. Bouchart, J.C. Hornez, A. Leriche, D. Hautcoeur, V. Lardot, F. Cambier, M.H. Fernandes, F. Monteiro, Osteoblastic cells colonization inside beta-TCP macroporous structures obtained by ice-templating, J. Eur. Ceram. Soc. 36 (2016) 2895–2901, https://doi.org/10.1016/j.jeurceramsoc.2015.10.030.
[24] K. Zhao, Y.-F. Tang, Y.-S. Qin, J.-Q. Wei, Porous hydroxyapatite ceramics by ice templating: freezing characteristics and mechanical properties, Ceram. Int. 37 (2) (2011) 635–639, https://doi.org/10.1016/j.ceramint.2010.10.003.
[25] M. Mellor, I. Hawkes, Measurement of tensile strength by diametral compression of discs and annuli, Eng. Geol. 5 (1971) 173–225, https://doi.org/10.1016/0013-7952(71)90001-9.
[26] S. Prakash Rao, Sushree S. Tripathy, Ashok M. Raichur, Dispersion studies of sub-micron zirconia using dolapix CE 64, Colloid surf, A-physicochem. Eng. Asp 302 (2007) 553–558, https://doi.org/10.1016/j.colsurfa.2007.03.034.
[27] K. Lu, C.S. Kessler, Optimization of a nanoparticle suspension for freeze casting, J. Am. Ceram. Soc. 89 (8) (2006) 2459–2465, https://doi.org/10.1111/j.1551-2916.2006.01111.x.
[28] S. Deville, E. Saiz, A.P. Tomsia, Freeze casting of hydroxyapatite scaffolds for bone tissue engineering, Biomaterials 27 (2006) 5480–5489, https://doi.org/10.1016/j.biomaterials.2006.06.028.
[29] D. Hautcoeur, M. Gonon, C. Baudín, V. Lardot, A. Leriche, F. Cambier, Alumina porous ceramics obtained by freeze casting: structure and mechanical behaviour under compression, Ceramics 1 (2018), https://doi.org/10.3390/ceramics1010008.
[30] S. Deville, Freeze casting of porous ceramics: a review of current achievements and issues, Adv. Eng. Mater. 2008 10 (3) (2007) 155–169, https://doi.org/10.1002/adem.200700270.
[31] R.W. Rice, Chapter 1: overview: porosity (and microcrack) dependence of properties, Porosity of Ceramics Properties and Applications, CRC Press, USA, 1998, pp. 1–42, https://doi.org/10.1201/9781315274539.
[32] L.J. Gibson, Biomechanics of cellular solids, J. Biomech. 38 (2005) 377–399, https://doi.org/10.1016/j.jbiomech.2004.09.027.
[33] D.R. Carter, G.H. Schwab, D.M. Spengler, Tensile fracture of cancellous bone, Acta Orthop. Scand. 51 (5) (1980) 733–741, https://doi.org/10.3109/17453678008990868.